

Received 30 August 2017; revised 17 November 2017; accepted 4 December 2017. Date of publication 20 March 2018; date of current version 9 April 2018. The review of this paper was arranged by Editor A. Nathan.

Digital Object Identifier 10.1109/JEDS.2018.2792311

Drift Field Implementation in Large Pinned Photodiodes for Improved Charge Transfer Speed

DONALD B. HONDONGWA^{1b} (Student Member, IEEE), AND ERIC R. FOSSUM (Fellow, IEEE)

¹Thayer School of Engineering, Dartmouth College, Hanover, NH 03755, USA

CORRESPONDING AUTHOR: D. B. HONDONGWA (e-mail: donald.b.hondongwa.th@dartmouth.edu)

This work was supported by Varex Imaging Corporation.

ABSTRACT We present a methodology for generating built-in drift fields in large photodiodes. With the aid of TCAD we demonstrate how non-uniform doping profiles can be implemented in a standard CMOS process using a single additional mask and controlled using the implant conditions and mask geometry. We demonstrate that the resulting doping profile creates a built-in drift field and simulates the effect of the drift field on the charge transfer speed. We show that implementing a drift field can improve charge transfer characteristics of the photodiode.

INDEX TERMS CMOS image sensors, pinned photodiodes, charge transfer, large photodiodes.

I. INTRODUCTION

The pinned photodiode has become the technology of choice for CMOS image sensors primarily due to its superior performance [1]. While the general trend has been toward smaller pixels and higher resolution, there is still a lot of interest in large pixels especially in scientific and medical imaging where there may be limited signal so large diodes are required to improve the signal to noise performance [2]–[4].

In large photodiodes, one of the design challenges is achieving fast and complete charge transfer which is essential in cases requiring high-speed low noise imaging. The speed of a pixel is determined by the speed of the readout electronics as well as the speed of its internal charge transfer. As the photodiode gets larger, the charge transfer time increases primarily because of the increased distance that the charge must travel [5].

Charge transfer is a complex process driven by a variety of coupled processes, including drift, diffusion and self-induced drift [6], [7]. It is believed that in the absence of an electric field, diffusion is the dominant factor and the transfer time is proportional to the square of the distance while in the presence of an electric field, the transfer time becomes proportional to the distance. An analysis of charge transfer in charge-couple devices (CCDs) was presented in [7]–[9] showing the influence of self-induced drift,

fringing fields and diffusion, and they conclude that the addition of an electric field improved that charge transfer speed. While the analysis was tailored to CCD gates, similar principles can be extended to charge transfer in the photodiode too.

Several methods have been proposed to improve the charge transfer speed in large photodiodes. The proposals have included shaping the diode [10]–[12], grading the diode implants, external biasing [13] or some combination of these [14]–[17]. Diode shaping has the disadvantage that it is complex to implement, and can potentially reduce fill factor as shown in [12] where the electric field is achieved at the expense of diode fill factor. Kosonocky *et al.* [18] demonstrated charge transfer speed improvements in pinned photodiode based CCD imager using a multi-step diode doping profile. Later, additional studies showed that increasing the number of doping levels further increased the speed [19]. Grading of doping implants has also been achieved by varying the thickness of the masking material [20]. The challenge with these methods presented for varying the doping implant is that while they improve the charge transfer speed, they are typically implemented using several additional masks, one for each doping level which increases the cost of fabrication.

A method for creating arbitrary doping profiles with a single implant was presented [21] and demonstrated for use in

photodiodes [22]. The proposed method works by dividing the diode into segments and creating a mask opening for each segment with a size determined by the desired profile. Following an implant step, a diffusion step is used to create the profile. The advantage of this method is that only a single mask is required to make the doping profile and this is a significant improvement over the other proposals that require an additional mask for each doping level. The method relies on, and is thus limited by, the geometric properties of the mask. The minimum concentration in the profile is dictated by the minimum allowed feature size, while the maximum is limited by the thermal budget.

We developed a method of implementing arbitrary doping profiles in diodes by taking advantage of modern CMOS processing and tilted implants. The focus shall be on creating monotonic, approximately linear doping profiles that will create potential profiles and improve the charge transfer characteristics in CMOS photodiodes. To this end, tilted implants are used to create the variations in doping concentration and a diffusion step is used to smooth the doping profile. We analyze the relationship between some sample doping profiles and the charge transfer speed using TCAD modeling. Using the implant tilt angle adds an extra degree of freedom to the profile creation process, removing the geometrically imposed restriction.

II. DOPING PROFILE

The proposed method relies on the implant conditions and mask geometry to create the desired doping profile. The angle and energy of the implants are used for precise placement of the dopants and we can take advantage of the shadowing/windowing of angled implants to create a doping profile. When the diode is viewed as being divided into a series of small segments, then the doping profile is given by the local average doping in each segment. This means, for example, to get a linearly increasing doping profile, we would design the local average concentration to be linearly increasing as well.

The average number of dopant particles implanted through a mask opening depends on the angle of the implant, an effect that can be described as window modulation or windowing. Due to the angle of the implant, the effective window size is geometrically altered as shown in Fig. 1. For an implant at angle θ from the vertical, through an opening window w , the effective window size can be shown to be given by Equation (1) where w is the geometric window width and w' is the effective window size.

$$w' = w - h \cdot |\tan(\theta)| \quad (1)$$

The local average doping concentration in the segment can be described by Equation (2), assuming that the doping is proportional to the window opening.

$$\text{local density (LD)} = C_p \frac{w'}{s} \quad (2)$$

where w' is as described in Equation (1), s is the segment size and C_p is a proportionality constant dependent on the

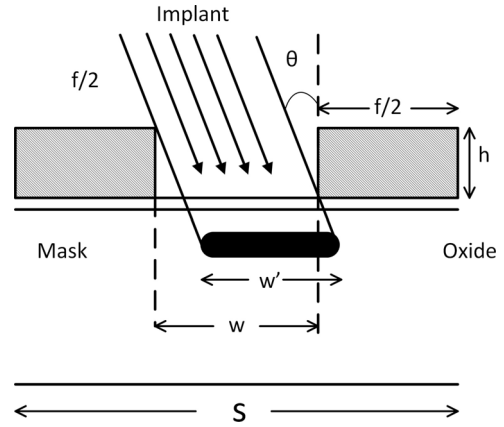


FIGURE 1. Schematic of dopants being implanted through an opening in a mask illustrating the shadowing effect.

implant dose, energy and thermal diffusions. C_p is the doping density when $w' = s$, i.e., when the mask is absent. The local density can thus be controlled by adjusting the ratio of the effective window size to the segment size which is a function of the implant angle and the mask geometry. It should be noted that both Equation (1) and (2) are first order approximations implicitly assuming that the mask completely blocks the implants. This is not the case for high energy implants through a thin mask and in the corners (top left and bottom right in Fig. 1) where effective thickness is reduced. In those cases, some of the implants will pass through the mask. However, the error introduced by this simplifying assumption will be small enough that the conclusion of the analysis still holds.

Analysis of Equation (1) shows that for some values of θ the effective window size can be zero, and in this case, none of the implant particles make it to the wafer. We can define an acceptance angle, θ_{max} , above which the effective window goes to zero. For a mask of thickness h and a window opening of width w we can define an aspect ratio $r_0 = \frac{w}{h}$ and the acceptance angle is given by Equation (3).

$$\theta_{max} = \tan^{-1}(r_0) \quad (3)$$

Equation (3) can be used to find the range of usable implant angles for a given set of geometric limits which are typically a function of the chosen fabrication process. It also shows that larger angles contribute more to wider openings than to narrower ones, a fact that can be used to create more complex profiles.

From this analysis, a strategy for implementing arbitrary doping profiles can be developed. The simplest implementation would be to choose one fixed angle and change the mask openings. In this case, the segment size s is described by Equation (4).

$$s = w + f \quad (4)$$

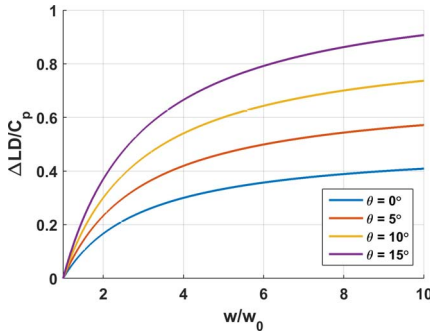


FIGURE 2. Doping differences as a function of the changing window size at various implant angles.

Here f is the feature size and w is the window opening. The Local Density, LD, is thus described by Equation (5).

$$LD = C_p \frac{w'}{w+f} = C_p \frac{w - |h \cdot \tan(\theta)|}{w+f} \quad (5)$$

Equation (5) is only valid for $\theta \leq \theta_{max}$, otherwise LD goes to zero. The equation shows that the resulting profile depends on both the mask geometry and the implant angles. For a fixed opening, LD can go to zero by increasing the angle or mask thickness, a feature that is not present in the method proposed in [21] in which lower limit is to the doping is set by the minimum achievable mask opening.

We can consider two openings of width w_0 and w_1 . The doping difference between the two can be calculated with Equation (6).

$$LD_1 - LD_0 = C_p \left(\frac{w'_1}{s} - \frac{w'_0}{s} \right) \quad (6)$$

For $\theta < \theta_{max}$, Equation (6) and Equation (1) result in Equation (7) where $\Delta LD = LD_1 - LD_0$. Equation (7) simplifies to Equation (8).

$$\frac{\Delta LD}{C_p} = \frac{w_1 - h \cdot |\tan(\theta)|}{w_1 + f} - \frac{w_0 - h \cdot |\tan(\theta)|}{w_0 + f} \quad (7)$$

$$\frac{\Delta LD}{C_p} = (f + h \cdot |\tan(\theta)|) \cdot \left(\frac{w_1 - w_0}{(w_1 + f)(w_0 + f)} \right) \quad (8)$$

Equation (8) shows that the doping difference between segments with different opening sizes depends on the angle, feature size and the mask thickness. Larger angles result in a steeper implant profile for the same mask geometry. For a fixed segment size, s , Equation (7) shows that the doping difference is only dependent on the mask geometry and not the implant angle. Fig. 2 shows how the doping difference changes as the window opening is scaled for various implant angles with $f = 0.22 \mu\text{m}$, $w_0 = 0.22 \mu\text{m}$, $h = 1.0 \mu\text{m}$.

III. EXTENSION TO 2D

The analysis presented describes the creation of one dimensional profiles, however, the theory can be extended to describe the creation of two dimensional profiles. The extension to 2D is based on the same principles of using mask

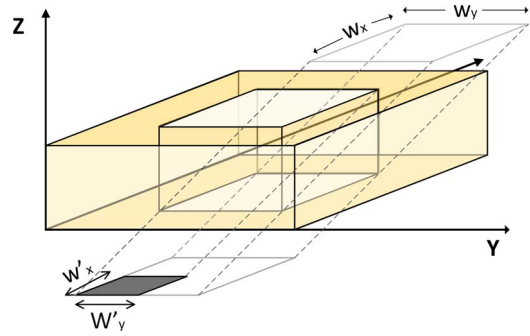


FIGURE 3. Implant through rectangular window showing the shadowing effect in two dimensions.

geometry and implant angles to create the initial profile and diffusion to smooth the implant.

In the case of two dimensional profiles, the effect of both the tilt from the vertical and the rotation of the implant relative to the mask opening must be considered when implementing the doping profile. Fig. 3 shows an implant through a rectangular opening. In this case, both the length and the width can be modulated by changing the tilt and the rotation. The effective window dimensions of the implant are given by Equations (9) and (10) where θ is the tilt from vertical tilt and φ is the azimuthal angle as measured from the x-axis.

$$w'_x = w_x - h \cdot \tan(\theta) \cdot \cos(\varphi) \quad (9)$$

$$w'_y = w_y - h \cdot \tan(\theta) \cdot \sin(\varphi) \quad (10)$$

The local density as described in Equation (2) transforms to an area average given by

$$LD = C_p \cdot \frac{w'_x \cdot w'_y}{S_x S_y} \quad (11)$$

As is the case with 1D analysis, the local density can be controlled by the mask geometry and the implant vertical tilt angle with horizontal rotation as an additional degree of freedom.

IV. SIMULATION

A series of simulation experiments were designed to demonstrate this methodology and investigate the speed improvements that could be achieved. The simulated fabrication process was based on a commercially available process for image sensors. The potential profile is first checked to ensure that there is no potential barrier between the photodiode and the floating diffusion. Such a barrier would result in incomplete charge transfer and lag which would affect the charge transfer measurements.

The net diode doping is the difference between the acceptor and donor concentrations, thus a net doping profile can be achieved by changing, either the acceptor concentration or the donor concentration. Because boron atoms are relatively small they have a high diffusivity constant and thus require smaller thermal budgets. We chose to create an inverse profile in boron instead of creating the profile using the donor

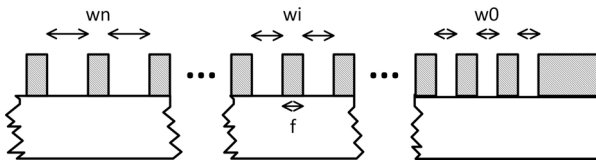


FIGURE 4. Masking strategy for one dimensional doping profile.

TABLE 1. Mask specifications.

W [μm]	S [μm]	L [μm]
0.22	0.44	43-48
0.24	0.46	38-43
0.26	0.48	33-38
0.28	0.50	28-33
0.30	0.52	23-28
0.32	0.54	18-23
0.34	0.56	13-18
0.36	0.58	08-13
0.38	0.60	03-08

dopants due to this property. This method also has the advantage that it does not affect the carefully crafted doping profile around the gate because the boron doping goes to zero. This provides a lot of freedom in the placement of the additional doping step in the processing lineup allowing it to be added to sections of the fabrication process that have minimal impact on the thermal budget.

The simulation was done for diodes 50 μm long and implants at $\pm 12.5^\circ$, $\pm 15^\circ$, $\pm 17.5^\circ$ degrees, and with no added implant for reference. Simulations of the photodiode without an implant profile were simulated as well for use as a bench mark. The boron implant was done at a dose of $5e11 \text{ cm}^{-2}$ and an energy of 35 keV and annealed at 1100 $^\circ\text{C}$ for 30 minutes. The mask for the doping is designed to meet the minimum specifications for a 0.18 μm fabrication process. We used a fixed window spacing, f , of 0.22 μm , just above the minimum feature size and a mask thickness (h) of 1 μm . The window width was varied by steps of 20 nm starting from 220 nm up to 380 nm to create ten doping levels. To cover the length of the diode, the diode was divided into roughly equal sections and in each section the window opening was kept constant, while the opening increased from section to section resulting in a staircase doping profile. Fig. 4 outlines the mask creation scheme and Table 1 shows the 9 sections of the diode, the window opening in each section and the corresponding segment size.

The charge transfer speed was then simulated for each of the devices. The photodiodes were first illuminated with light at 550 nm while the transfer gate was off. The transfer gate was then turned on while the reset transistor was on and the decay of the charge in the photodiode with time is observed as the charge is transferred to the floating diffusion (FD). To avoid corrupting the measurements with concerns about FD capacity and differences in full well capacities, the charge transfer speed is calculated from the charge density decay

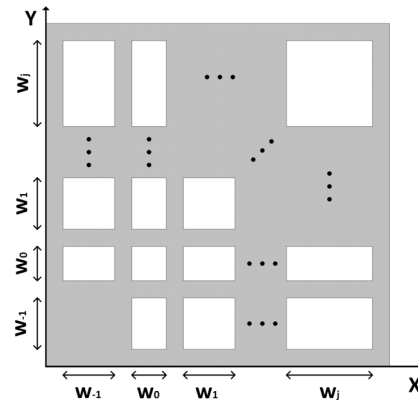


FIGURE 5. Drawing of mask for 2D profile showing how the geometry of the openings change.

in the photodiode when the transfer gate is enabled and the reset gate is on.

To test the 2D extension of the process, we performed a 3D implant and diffusion simulation in TCAD. The mask was generated with rectangular openings whose length varies in the x-direction and the width was varied in the y-direction as shown in Fig. 5. In this case $W_i > W_{i-1}$ for all $i \geq 1$. W_{-1} was set to be larger than W_0 . The aim was to see if we could generate a doping profile in the two dimensions. The implant was performed at $\pm 17.5^\circ$ tilt, and 45° rotation measured counter-clockwise from the x-axis. 3D simulations were attempted with 50 μm pixels, however the required computational resources overloaded our computer systems. As a result, the device was limited to 10 μm .

V. RESULTS AND DISCUSSION

Fig. 6 shows the 1D doping profile created using the various conditions with the floating diffusion at $x = 49.5 \mu\text{m}$. The resulting profile created from linearly increasing mask sizes is not linear as predicted by Equation (8). For comparison, Fig. 6 is the model results from Equation (5) for an implant at 12.5° with $C_p = 1.45e16 \text{ cm}^{-3}$ and an offset of about $3.4e15 \text{ cm}^{-3}$ shift to account for the fact that the photoresist is not completely blocking. Also, worth noting in Fig. 6 is the fact the diodes have the same doping around the transfer gate, the addition of the doping profile did not affect the doping in that region.

1D cutlines of the potential profiles for the various implant conditions are shown in Fig. 7 and Fig. 8 shows a surface plot of the potential for the 12.5° implant conditions. The electrostatic potential is shown when the photodiode is empty and is thus showing the profile of the pinning level. The pinning level is changing with the doping level as expected.

To investigate the charge transfer speed, the charge density in the photodiode was monitored when the transfer gate is opened. Fig. 9 shows a plot of the integral of the charge density for a width of 50 μm versus time.

The addition of a non-uniform doping profile greatly reduces the charge transfer time. The presence of a potential profile improves the charge transfer speed of the diode

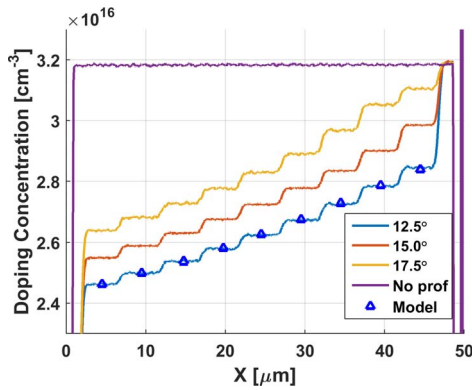


FIGURE 6. The net doping profiles created with implants at various angles from simulation and from the model. FD at $x = 49.5 \mu\text{m}$.

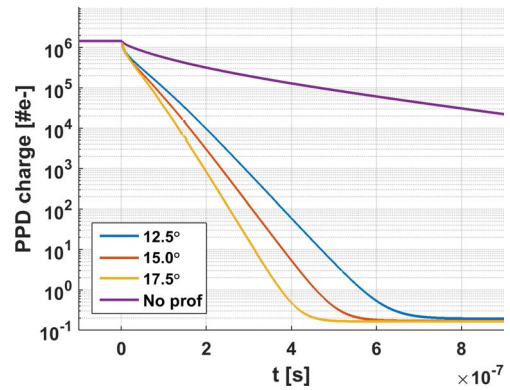


FIGURE 9. Charge decay from PPD when the TG gate is turned on at $t = 0$ s.

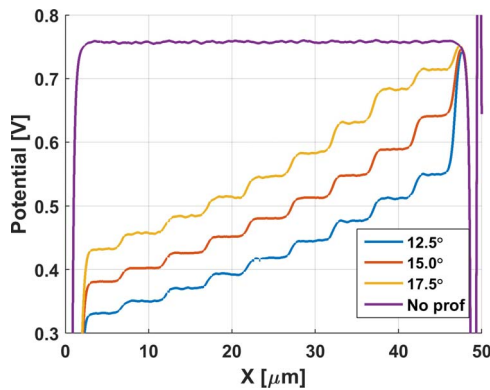


FIGURE 7. The potential profiles resulting from the doping profiles.

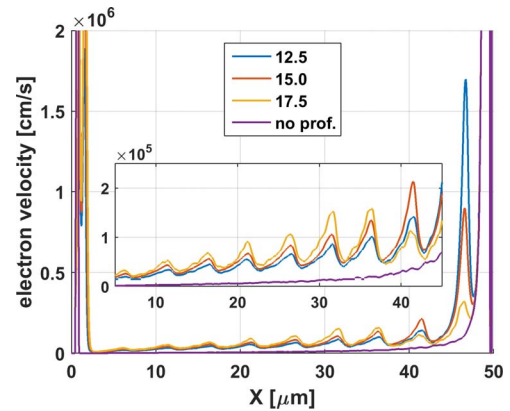


FIGURE 10. Electron velocity along the diode length. The location pulses in velocity correspond to the potential steps.

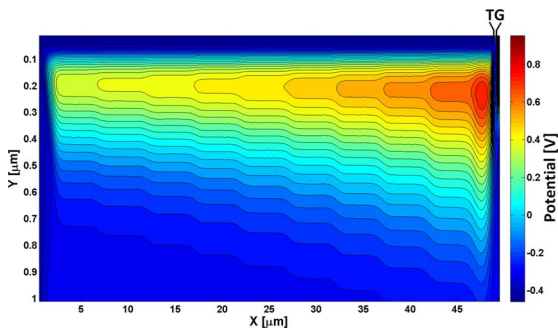


FIGURE 8. Surface plot of the potential for 12.5° angled implant.

as expected. This is because adding the potential profile increases the drift velocity and improves charge transfer. To compare the transfer time improvements, we calculated the decay time constant (τ) of the charge density after the transfer gate is turned on. The time constant, τ , was calculated as the inverse of the slope on the curve of the natural logarithm of the PPD charge with time. The results are tabulated in Table 2.

Fig. 10 shows the electron velocities along the profile when the TG gate is on. One might expect that the profile with the highest average electron velocity would have the fastest transfer time.

If the average of the electron velocity is calculated over the length of the PPD, the 12.5° implant has the highest average, but simulations show it has the slowest transfer time. This would suggest that the profile of the electron velocity in addition to the average electron velocity affects the transit time. A comparison of the profiles show that the 12.5° implant had a low electron velocity for much of the diode length with a huge spike at the end. This is contrary to the 17.5° implant which had a higher velocity for much of the diode, but no spike at the end. We hypothesize that in the case of the 12.5° implant, even though the average velocity is higher, there is a speed limit at the beginning of the diode. Like a water fall, no matter how high the water fall is, if the upstream speed is limited, then the rate at which water falls off the edge is limited as well.

To account for the shape of the profile, one can model the average transit time with Equation (12).

$$t = \int_{x_0}^{x_0+L} \frac{1}{v(x)} dx \quad (12)$$

Here t is the average time a particle at x_0 would take to get to $x_0 + L$ where the electron velocity is described by $v(x)$. For the three profiles, we calculated t for $x_0 = 3 \mu\text{m}$ and $L = 44 \mu\text{m}$ and the results are also tabulated in Table 2.

TABLE 2. Results of charge transfer simulations where τ is the characteristic decay time of the charge transfer and t is the average transit time as described in Eqn 12.

Angle	τ [ns]	t [ns]
No Profile	206	1148
12.5	40.0	126
15.0	31.9	105
17.5	25.0	90.7

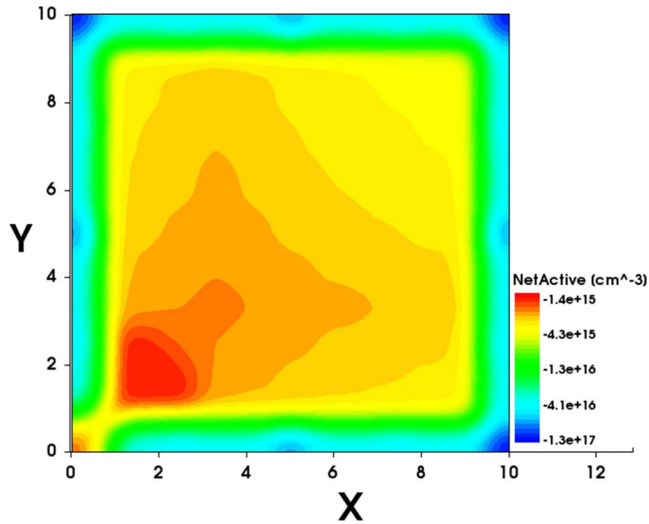


FIGURE 11. Two-dimensional doping profile created using the proposed method. The net doping increases from the upper right corner to the bottom left corner.

The doping profile created from the 3D simulation is shown in Fig. 11. The doping profile is expected based on the theory presented. The boron concentration is reduced as the area of the mask opening is reduced. This kind of profile can be used to funnel charge to the upper right corner, where the TG gate can be placed.

VI. CONCLUSION

We have presented a means of creating non-uniform doping profiles using a single mask by utilizing the implant angle to accurately control the profile. We have shown how including the tilt angle as a design parameter can increase design flexibility. A model describing the procedure has been provided and sample profiles were demonstrated using TCAD tools. The results of the simulations match the model estimates. The doping profile has been shown to improve the charge transfer speed in large photodiodes. Future work will include investigating different profiles to optimize the charge transfer and investigate how the shape of the profile affects the transfer speeds further.

ACKNOWLEDGMENT

The authors would like to thank Varex Imaging Corporation for funding support. They also appreciate the technical discussions with other members of the group especially J. Ma and D. Starkey

REFERENCES

- [1] A. Theuwissen, "CMOS image sensors: State-of-the-art and future perspectives," in *Proc. ESSCIRC 33rd Eur. Solid-State Circuits Conf.*, Munich, Germany, 2007, pp. 21–27.
- [2] L. Korthout *et al.*, "A wafer-scale CMOS APS imager for medical X-ray applications," in *Proc. Int. Image Sensor Workshop*, Bergen, Norway, 2009. [Online]. Available: http://www.imagesensors.org/Past%20Workshops/2009%20Workshop/2009%20Papers/070_paper_korthout_dalsa_wsc.pdf
- [3] R. Turchetta, N. Guerrini, and I. Sedgwick, "Large area CMOS image sensors," *J. Instrum.*, vol. 6, no. 1, 2011, Art. no. C01099.
- [4] D. Scheffer, "A wafer scale active pixel CMOS image sensor for generic X-ray radiology," in *Proc. SPIE*, vol. 6510. San Diego, CA, USA, 2007, Art. no. 65100O.
- [5] A. Pelamatti *et al.*, "Charge transfer speed analysis in pinned photodiode CMOS image sensors based on a pulsed storage-gate method," in *Proc. 45th Eur. Solid State Device Res. Conf. (ESSDERC)*, Graz, Austria, 2015, pp. 156–159.
- [6] E. R. Fossum and D. B. Hondongwa, "A review of the pinned photodiode for CCD and CMOS image sensors," *IEEE J. Electron Devices Soc.*, vol. 2, no. 3, pp. 33–43, May 2014.
- [7] A. J. Theuwissen, *Solid-State Imaging With Charge-Coupled Devices*, vol. 1. Amsterdam, The Netherlands: Springer, 1995.
- [8] J. E. Carnes, W. F. Kosonocky, and E. G. Ramberg, "Free charge transfer in charge-coupled devices," *IEEE Trans. Electron Devices*, vol. 19, no. 6, pp. 798–808, Jun. 1972.
- [9] Y. Daimon, A. M. Mohsen, and T. C. McGill, "Final stage of the charge-transfer process in charge-coupled devices," *IEEE Trans. Electron Devices*, vol. 21, no. 4, pp. 266–272, Apr. 1974.
- [10] B. Shin, S. Park, and H. Shin, "The effect of photodiode shape on charge transfer in CMOS image sensors," *Solid-State. Electron.*, vol. 54, no. 11, pp. 1416–1420, 2010.
- [11] Y. Xu and A. J. P. Theuwissen, "Image lag analysis and photodiode shape optimization of 4T CMOS pixels," in *Proc. Int. Image Sensor Workshop*, 2013, pp. 153–157.
- [12] H. Takeshita, T. Sawada, T. Iida, K. Yasutomi, and S. Kawahito, "High-speed charge transfer pinned-photodiode for a CMOS time-of-flight range image sensor," in *Proc. SPIE Sensors Cameras Syst. Ind. Appl. XI*, vol. 7536. San Jose, CA, USA, 2010, Art. no. 75360R.
- [13] S.-M. Han *et al.*, "A time-of-flight range image sensor with background canceling lock-in pixels based on lateral electric field charge modulation," *IEEE J. Electron Devices Soc.*, vol. 3, no. 3, pp. 267–275, May 2015.
- [14] X. Cao *et al.*, "Design and optimisation of large 4T pixel," in *Proc. Int. Image Sensor Workshop (IISW)*, 2015, pp. 112–115.
- [15] R. Mahdi, J. Fink, and B. J. Hosticka, "Lateral drift-field photodetector for high speed 0.35 μm CMOS imaging sensors based on non-uniform lateral doping profile: Design, theoretical concepts, and TCAD simulations," in *Proc. Conf. Ph. D. Res. Microelectron. Electron. (PRIME)*, 2010, pp. 1–4.
- [16] C. Tubert *et al.*, "High speed dual port pinned-photodiode for time-of-flight imaging," in *Proc. IISW*, 2009, pp. 1–3.
- [17] K. Miyauchi *et al.*, "Pixel structure with 10 nsec fully charge transfer time for the 20m frame per second burst CMOS image sensor," in *Proc. IS&T/SPIE Electron. Imag.*, 2014, pp. 902203–902212.
- [18] W. F. F. Kosonocky *et al.*, "360x360-element very-high-frame-rate burst image sensor," in *Proc. IEEE Int. Solid-State Circuits Conf.*, San Francisco, CA, USA, 1996, pp. 182–183.
- [19] T. Kundu, R. K. Jarwal, and D. Misra, "Electron transit time enhancement in photodetectors for high speed imaging," in *Proc. 32nd Eur. Solid-State Device Res. Conf.*, vol. 2002. Florence, Italy, 2002, pp. 651–654.
- [20] M. Monoi *et al.*, "A single-layer CCD image sensor with wide gap electrode and gradual potential channel," in *Proc. SPIE Sensors Cameras Syst. Ind. Sci. Appl. X*, vol. 7249. San Jose, CA, USA, 2009, Art. no. 72490I.
- [21] S. Merchant, "Arbitrary lateral diffusion profiles," *IEEE Trans. Electron Devices*, vol. 42, no. 12, pp. 2226–2230, Dec. 1995.
- [22] D. Durini *et al.*, "Lateral drift-field photodiode for low noise, high-speed, large photoactive-area CMOS imaging applications," *Nucl. Instrum. Methods Phys. Res. A Accelerators Spectrometers Detectors Assoc. Equipment*, vol. 624, no. 2, pp. 470–475, 2010.



DONALD B. HONDONGWA (S'12) received the B.A. degree in physics from Vassar College, Poughkeepsie, NY, USA, in 2011 and the B.E. degree from the Thayer School of Engineering, Dartmouth College, Hanover, NH, USA, in 2012.

He is currently pursuing the Ph.D. degree with the Thayer School of Engineering, focusing on advanced imaging technologies, CMOS image sensor design, photon counting, and imaging applications.



ERIC R. FOSSUM (S'80–M'84–SM'91–F'98) is a Professor with the Thayer School of Engineering, Dartmouth College. He is the primary inventor of the CMOS image sensor used in billions of smart phones and other applications. He was inducted into the National Inventors Hall of Fame. He was a recipient of 2017 Queen Elizabeth Prize Laureate. He was elected to the National Academy of Engineering, among other honors. He is currently researching the Quanta Image Sensor and other photon-counting image sensors.